arXiv:astro-ph/0406212v2 19 Oct 2004

Comparison of Radio Observations and Numerical Simulations of the Radio Lobes of Cygnus A

Joel C. Carvalho

Space Telescope Science Institute, 3700 San Martin Dr., Baltimore, MD 21218

carvalho@dfte.ufrn.br

Ruth A. Daly

Department of Physics, Berks-Lehigh Valley College, Penn State University, Reading, PA 19610

rdaly@psu.edu

Matthew P. Mory

Department of Physics, Berks-Lehigh Valley College, Penn State University, Reading, PA 19610

mmory@srtedg.com

and

Christopher P. O'Dea

Department of Physics, Rochester Institute of Technology, 54 Lomb Memorial Drive, Rochester, NY 14623

odea@cis.rit.edu

ABSTRACT

We present a comparison of radio observations of the archetypal powerful radio galaxy Cygnus A and 2-D numerical hydrodynamical simulations. We characterize some global trends in the observed radio properties and compare them with the properties of a simulated radio source. The observational results are the following. The width of the observed surface brightness distribution perpendicular to the source axis can be well characterized by a Gaussian over most

[1]Departamento de Fisica, UFRN, C.P. 1661, CEP 59072-970, Natal, RN, Brazil

of the length of the source. The ratio of the Gaussian FWHM to the second moment is fairly constant along the source with an average value of about 2.5 indicating that they give roughly consistent measurements of the source width. The average observed surface brightness, estimated pressure, and estimated minimum energy B field decrease with distance from the hot spots. We find evidence for significant structure in the estimated cross-sectional slices of emissivity. The numerical results are the following. Jets propagating in a constant density atmosphere will decelerate with time. Thus, the estimated dynamical age of the source will be greater than the actual age of the source. For a source similar to Cygnus A the difference will be about a factor of 2. The second moment gives an accurate representation of the "true" width of the simulated source. The Gaussian FWHM tends to be about 40% larger than the true width and can be systematically in error if the surface brightness exhibits multiple peaks. We suggest that the ratio of the Gaussian FWHM to the second moment may be a diagnostic of the emissivity profile in the lobes. The simulations can qualitatively reproduce the overall observed morphology and the behavior of the cross-sections in surface brightness, the decline in surface brightness with distance from the hot spots, and the width of the lobes. This suggests that the 2-D simulations give a reasonable representation of the properties of Cygnus A.

Subject headings: galaxies: jets – galaxies: intergalactic medium – hydrodynamics – radio continuum: galaxies

1. Introduction

The primary physical processes in large, powerful FRII radio galaxies are still poorly understood. There is a consensus that the sources are powered by two oppositely directed, highly collimated outflows from an AGN - resulting in shocks and radio emission (Scheuer 1974; Blandford & Rees 1974). It is clear that the youngest populations of relativistic electrons are located near the radio hotspots at the extremities of the source (e.g., Leahy, Muxlow, & Stephens 1989; Carilli et al. 1991; Alexander & Leahy 1987). Beyond this, differences of opinions begin to emerge.

It is important to understand the physical processes that shape the observed radio emission of a source. If these could be identified and understood, it might be possible to use the observed source properties to determine the pressure, density, and temperature of the ambient gas, and the beam power of the source. These could then be used to probe the evolution of source environments with redshift, and evolution of AGN properties, such as jet

power. These, in turn, would suggest the circumstances that lead to AGN activity, and the role of environment in both triggering (perhaps via mergers or close encounters) and then constraining (through the gaseous environment) the radio properties of a source.

Much effort has been spent on analysis of multi-frequency radio observations of radio galaxies (e.g., as summarized in Leahy 1991), and independently on numerical simulations of radio galaxies (e.g., Norman et al. 1982; Lind et al. 1989; Clarke, Norman & Burns 1989; Hardee & Norman 1990; Falle 1991; Clarke & Burns 1991; Cioffi & Blondin 1992; Loken et al. 1992; Mioduszewski, Hughes & Duncan 1997; Marti et al. 1997; Komissarov & Falle 1997, 1998; Rosen et al. 1999; Carvalho & O'Dea 2002a,b).

Here we attempt to bridge these two fields by directly comparing radio images of the archetypal radio galaxy Cygnus A with the results of 2-D hydrodynamical simulations of a source which is expected to be similar to Cygnus A. Our goal is to explore the behavior of global observed properties and relate these to intrinsic properties of the underlying flows.

2. Radio Observations & Data Analysis

Two observations of Cygnus A are studied in detail. The 151 MHz radio image from Leahy, Muxlow, & Stephens (1989) was kindly provided to us by Paddy Leahy, and the 1345 MHz image from Carilli et al. (1991), was kindly provided to us by Chris Carilli. The 151 MHz image, obtained with MERLIN, has an angular resolution of 3 arcsec down and mean and rms noise levels of 0.1 and 0.3 Jy/beam. The 1345 MHz image, obtained with the VLA, has an angular resolution of 1.36 arcsec down to mean and rms noise levels of 0.01 and 0.01 Jy/beam.

2.1. Surface Brightness Profiles and Gaussian Widths

The FITS images of the source at 151 and 1345 MHz were rotated in an identical manner so the hot spots lie on a horizontal line. The hot spot-hot spot axis was taken to be a symmetry axis of the source. Using AIPS and auxiliary programs, vertical slices of surface brightness perpendicular to the hot spot symmetry axis were taken at one pixel intervals of the FITS image, as illustrated in Figure 1. Each surface brightness profile was then studied in detail. Distances to each slice are measured in arc seconds relative to the hot spot on each side of the source, increasing as we move in toward the source center.

Each slice profile was fit with a Gaussian curve to determine the FWHM of the best fitting Gaussian. In these fits, we included the radio data above a threshold of the mean plus

three times the rms noise level of each image; data below this level were removed. These cuts were taken at 1 Jy/beam for the 151 MHz image and 0.04 Jy/beam for the 1345 MHz image.

The radio surface brightness profiles and best fit Gaussian curves are shown at integer intervals of 3 arc seconds (the FWHM of the 151 MHz image), in Figures 2, 3, 4, 5 for the 151 and 1345 MHz data, and for each side of the source.

Generally, the Gaussian fits provide a good fit to the profiles; occasionally the edges of the profiles drop more steeply than the wings of the Gaussian fit.

The full width at half maximum of these Gaussian fits are shown as a function of slice distance from the hot spot at 151 and 1345 MHz in Figure 6. The errors on the Gaussian widths are much smaller than the FWHM of the radio observations, so the one sigma error bar on the FWHM of the Gaussian was taken to be half of the FWHM of the observing beam. Thus, an uncertainty of 1.5 arc seconds for the 151 MHz data, and 0.7 arc seconds for the 1345 MHz data was adopted as the uncertainty of the Gaussian widths.

The ratio of the best fit Gaussian widths at 151 and 1345 MHz are shown in Figure 7. The fact that this ratio is unity over most of the source is reassuring, and suggests that to first order the 151 and 1345 MHz data define similar source shape and structure. The average value of the ratio for the left and right hand sides of the source, respectively, are $W_{151}/W_{1345} = 0.94 \pm 0.01$ and 0.90 ± 0.01 when all the data are included; when only data with hot spot distances between 6" and 48" are included these average value are 0.92 ± 0.01 and 1.01 ± 0.01 for the left and right sides of the source, respectively.

2.2. The First and Second Moments

Two other measures of source structure are the first and second moments of the cross-sectional surface brightness profiles described above. These were obtained using the standard expressions $\bar{x} = \sum(x_i\ S_i)/\sum(S_i)$, and $\sqrt{\sum(S_i\ [x_i - \bar{x}]^2)/\sum(S_i)}$, where S_i is the surface brightness at the point x_i, shown as the surface brightness and x-axis in Figures 2 to 5. These are plotted as a function of the slice distance from the hot spot in Figures 8 and 9. The uncertainty of the first moment is taken to be half the beam width, as above.

The first moment is a measure of the location of the surface brightness weighted central axis of the source. In the 151 and 1345 MHz data, we see a varying displacement (or wandering) of the surface brightness weighted source axis which is small compared with the Gaussian FWHM of the bridge at similar bridge locations. The first moment can be affected

by the jet that is apparent in the radio grey scale images, and it is interesting that the deviations of the first moment from zero (expected for a perfectly cylindrically symmetric source) are in opposite sense for the right and left-hand side of the source, which could be influenced in part by any wobbling of the outflow axis of the jets. A detailed analysis indicates, however, that there is not an exact correspondence between the deviations of the first moment on each side of the source.

The second moment is another measure of the bridge width, and is shown in Figure 9. The bridge width as measured by the best fit Gaussian and the second moment are compared in Figure 10, which shows the ratio on the best fit Gaussian FWHM to the second moment. For the 151 MHz data, this ratio is 2.59 ± 0.07 for the left side of the source and 2.49 ± 0.07 for the right side of the source, while for the 1345 MHz data, this ratio is 2.45 ± 0.03 and 2.53 ± 0.03 for the left and right hand sides respectively. The fact that the ratio is similar over most of the source suggests that either method may be used to estimate the bridge width. The physical interpretation of the numerical value of the ratio is discussed in §3 (numerical simulations). Note that the ratio W_G/W_2 discussed in §3.4, obtained from the numerical simulations, is half of the value stated here since W_2 is twice the bridge radius indicated by the second moment.

2.3. The Average Surface Brightness Along the Bridge

The average surface brightness of each cross-sectional surface brightness profile is shown in Figure 11. This is obtained by summing up the total area under a particular surface brightness profile (see Figures 2 to 5) and dividing by the FWHM of the best fit Gaussian curve, W_G: $\bar{S} = \sum(S_i \Delta x)/W_G$, where S_i is the surface brightness for the ith point, Δx is the interval along x around the point i. Thus, the units of the average surface brightness are Jy/beam. Numerical simulations (see §3) indicate that W_G is a good estimate of the bridge diameter, suggesting that the surface brightness values obtained and shown in Figure 11 do not need to be re-normalized.

The uncertainty of the average surface brightness is obtained by adding the rms noise level of the image in quadrature with the beam width: $(\delta\bar{S}/\bar{S})^2 = (rms/\bar{S})^2 + (\theta_b/2W_G)^2$, where θ_b is the FWHM of the observing beam; recall that the uncertainty on the Gaussian width is taken to be half the beam size.

The contrast between the hot spots and the bridge is much higher for the 1345 MHz data than it is for the 151 MHz data, and the values of $\bar{S}$ differ substantially for the data sets. But, once we move beyond the hot spots into the bridge region, the profile of the

average surface brightness along the bridge axis is similar for the two frequencies, which can be seen in Figure 11.

2.4. The Average Pressure and Minimum Energy Magnetic Field Along the Bridge

The average bridge pressure for each slice is plotted as a function of distance from the hot spot on each side of the source in Figure 12. This is a "minimum energy" pressure (Burbidge 1956) in the sense that it is obtained using the equation $P = (\bar{S}/W_G)^{4/7}$ (see Figures 2 to 5). Thus, the pressure has units of (Jy/arc sec)$^{4/7}$. To convert this to physical units of erg/cm^3 and thus obtain the normalization factor to apply to the pressure presented, we note that the pressure is simply related to the minimum energy magnetic field (e.g. Wan et al. 2000): $P = (1.33b^{-1.5} + b^2)B^2/(24\pi)$, where B is the minimum energy magnetic field strength and b parameterizes the offset from minimum energy conditions: the true field strength is bB. As described below, the minimum energy magnetic field strength estimated using the 151 MHz data has a normalization factor of 30μG, so the normalization factor for the pressure estimated using the 151 MHz data is about 1.2×10^{-11} erg cm$^{-3}(1.33b^{-1.5} + b^2)$, or about 2.8×10^{-11} erg cm^{-3} for $b = 1$, or about 1.3×10^{-10} erg cm^{-3} for $b = 0.25$, as suggested by Carilli et al. (1991), and confirmed by Wellman, Daly, & Wan (1997a,b) for the bridge region of Cygnus A. At 1345 MHz the normalization factor for the pressure is 10^{-10} erg cm$^{-3}(1.33b^{-1.5} + b^2)$, or about 2.4×10^{-10} erg cm^{-3} for $b = 1$, or about 1.1×10^{-9} erg cm^{-3} for $b = 0.25$.

It is clear from Figure 12 that the minimum energy magnetic fields computed for the bridge region using the 151 MHz and 1345 MHz data are similar in magnitude and structure, while the pressures computed for the hotspots are considerably different - with the 1345 MHz data indicating a much higher pressure than the 151 MHz data.

The average minimum energy magnetic field strength is each slice is obtained by taking the square root of the minimum energy pressure, $B = (\bar{S}/W_G)^{2/7}$. The normalization factor is obtained using the standard expression for the minimum energy magnetic field strength, assuming zero energy in relativistic protons, a filling factor of unity, a constant spectral index of unity, frequency cut offs of 10 MHz and 100 GHz, and a cosmology with a value of Hubble's constant of 70 km/s/Mpc, a normalized mean mass density today of $\Omega_m = 0.3$, and a cosmological constant of $\Omega_\Lambda = 0.7$. These parameters yielded a normalization for the minimum energy magnetic field strength for the 151 MHz data of about 30μG, and a normalization factor of about 88μG for the 1345 MHz data. The minimum energy magnetic field strengths are shown in Figure 13. Like the minimum energy pressure, the minimum

energy magnetic field strengths across the bridge computed using the 151 MHz and 1345 MHz data are quite similar in magnitude and structure, while the hotspot magnetic field indicated by the 1345 MHz data is much larger than that indicated by the 151 MHz data. One of the reasons that the estimated pressures in the radio hot spots at 151 MHz and 1345 MHz differ is that the magnetic field strengths and hence pressures have been estimated assuming a constant spectral index of unity. While this may be a reasonable estimate in the bridge region of the source, it clearly is not a good approximation in the hot spot region.

Note that the total pressure P in relativistic electrons and fields estimated assuming that this pressure is proportional to the square of the minimum energy magnetic field implies that $P \propto (\epsilon)^{4/7}$, where ϵ is the volume emissivity of the radio emission (see §2.5). This follows from the fact that the radio surface brigthness S is obtained by integrating the emissivity along the source path length, so $\bar{S} \sim \epsilon W_G$. Thus, $P = (\bar{S}/W_G)^{4/7}$, which follows directly from the minimum energy argument, implies that $P \propto \epsilon^{4/7}$. This is a good approximation whenever the true field strength is proportional to the minimum energy magnetic field with a proportionality constant that is independent of position in the source.

2.5. The Radio Emissivity as a Function of Position

The emissivity, or energy emitted per unit volume per unit time at one particular frequency can be obtained from the surface brightness profiles shown in Figures 2 to 5. For a particular surface brightness profile, it is assumed that the emission is cylindrically symmetric, and that the diameter of the cylinder is equal to the total width of that profile (only data above the noise level of 1*mean + 3 rms are included). Then, the emissivity as a function of radius from the center of the slice can be determined. This is done in the following way. The data point that is furthest from the center of the slice with a surface brightness above the noise level is used to determine the edge of the source. We move in an amount Δx to the position that is centered on R_1, and compute the emissivity ϵ_1 at the point R_1 by taking the surface brightness at this point divided by the length of the chord through the circle that that point, as illustrated in Figure 14. We then have the emissivity ϵ_1 at all points that are at this distance, R_1, from the center of the cylinder for that slice. Stepping in, the next surface brightness data point can be used to determine the emissivity ϵ_2 that is a distance R_2 from the center of the circle; this is done by accounting for the fact that the total surface brightness S_2 will have contributions from ϵ_1 and ϵ_2, illustrated in Figure 14. This process is continued to obtain the emissivity as each distance R_n from the center of the axis of symmetry of the source, and is valid to the extent that the slice possesses cylindrical symmetry.

The normalization for the volume emissivity $\epsilon_\nu \equiv dE/(dV\ dt\ d\nu)$ can be obtained by noting that the emission coefficient $j_\nu = \epsilon_\nu/(4\pi)$ for a volume element that emits isotropically, and the specific intensity $I_\nu = j_\nu \Delta y$, where Δy is the length of the ray through the source that is shown in Figure 14. The observed specific intensity $I_{\nu_o} = I_\nu(1+z)^{-3}$, and has units of Jy/beam. Using these expressions it is easy to show that the normalization factor for the emissivities shown in Figures 15, 16, 17, and 18 are 1.8×10^{-34} erg s^{-1} cm^{-3} Hz^{-1} for the 151 MHz data, and 9.0×10^{-34} erg s^{-1} cm^{-3} Hz^{-1}.

These emissivities show significant structure, indicating that in any given slice there can be regions with very high and/or very low emissivities (or that the assumption of cylindrical symmetry was not a valid assumption for that slice). A relatively large change in emissivity is needed to produce a relatively small surface brightness feature. Some of the changes in emissivity are suggestive of a channel or jet-like feature, which are suggested by either an emission feature, or a cavity in the emissivity near the center of the slice. The variations in emissivity could be due to variations from cylindrical symmetry, hydromagnetic waves, turbulence, or other effects.

3. Cygnus A *versus* Numerical Simulations

Here we present the results of 2-D numerical hydro simulations and compare them with the observational results for Cygnus A. The advantage is that in the simulations we know the *intrinsic* properties of the "source". The disadvantage is that the simulations may not include all the relevant physics which occurs in real radio galaxies.

3.1. The Numerical Simulations

We have carried out axisymmetrical hydrodynamical numerical simulations of light jets propagating in a constant density atmosphere. The details of the simulations are discussed by Carvalho & O'Dea (2002a,b). We have chosen not to include magnetic fields in the simulations. If the magnetic field is dominant, MHD simulations produce structures (e.g., the "nose cone", Clarke et al 1986; Lind et al. 1989) which do not appear to correspond to the observed radio structures in Cygnus A. If the magnetic field is not dominant, the overall structure and dynamics of the source in the MHD simulation are similar to the case where the magnetic field is absent . In addition, in a particle pressure dominated source the magnetic field distribution closely follows the distribution of gas pressure and density (Lind et al 1989). Numerical simulations by Komissarov (1989) show that if the magnetic field is

initially weak, it will come into equilibrium with the gas pressure near the cocoon boundary because the gas pressure drives the sideways expansion of the cocoon, and the gas is not able to cross the magnetic field lines.

Numerical simulations studies (e.g., Norman et al. 1982; Carvalho & O'Dea 2002a,b; Krause 2003) indicate that light jets will inflate a cocoon whose width is inversely proportional to the density ratio (η) between the jet and the ambient gas. The over expanded bridge in Cyg A implies a very low value for η ($< 10^{-3}$). According to Alexander and Pooley (1996) an order-of-magnitude estimate of the jet density gives $\eta \sim 4 \times 10^{-5}$. We have run a number of simulations where we used $\eta = 2 \times 10^{-4}$ and a jet internal Mach number $M = 10$ (Run D01), $\eta = 1 \times 10^{-4}$, $M = 11$ (Run D02) and $\eta = 1 \times 10^{-4}$, $M = 10$ (Run D03). One of the reasons for doing so is to ensure that small changes on the jet parameters do not have a significant effect on the final results. Since the overall linear size of Cyg A is ~ 120 kpc we used a simulation grid with physical dimension 66 kpc in the direction of the source axis and a jet radius 1 kpc. We expect that, as the bow shock in front of the jet head reaches the end of the grid, the expanded cocoon would give a fair representation of the source lobe. We have run the simulations with several different grid widths (equivalent to 16.5, 33 and 49.5 kpc) in order to study the effect on the cocoon of the bow shock leaving the grid. In the largest grid (Run D01), the entire source is contained on the grid, while in the smaller grids, the bow shock eventually leaves the grid laterally. We find that the details of the cocoon properties differ in these simulations, though the overall properties of the cocoons are similar. This gives us confidence in the results of simulations carried out in the narrower grids which are computationally much cheaper.

The final stage of the simulation of Run D01 is shown as a density contour map in Fig. 19. After comparing this with Runs D02 and D03 we concluded that no significant change is observed in the source physical properties although their general appearance may look different. Therefore, in what follows we show the results for Run D01 only. In Fig. 20a we show the contours of the bow shock, cocoon and jet. Fig. 20 also shows the average pressure inside the cocoon (b) the lateral expansion speed of the cocoon (measured at the contact discontinuity) (c) and the lateral expansion speed of the bow shock (measured at the outer shock front) (d) along the source axis.

The average pressure was obtained in the following way. For each slice, with width equal to the grid cell and having cylindrical symmetry, the total thermal energy was calculated by summing up the product of the energy density per cell times the volume element of the cell, and then dividing by the total volume of the slice to obtain the total internal energy density, $0.5\rho v_{rms}^2$ or $3/2nkT$. This was then multiplied by $(\Gamma - 1)$ to obtain the average pressure in that cell. The simulations was carried out for a monotonic, ideal, non-relativistic fluid, thus

ratio of specific heats is $\Gamma = 5/3$.

The shock structure seen in the numerical simulation is shown in Figure 20a. As usual, three shock regions can be identified: the outer shock front, the contact discontinuity, and the inner shock, which includes the entire bridge region.

In the simulation, the location of the jet can also be identified. The outer shock front is also called the bow shock, and is indicated by the outermost line in Figure 20a. The contact discontinuity separates the shocked ambient gas from the shocked jet fluid and is indicated by the middle line in Figure 20a. The radio emitting fluid that would produce the observed radio emission is expected to lie within the contact discontinuity. Thus, the region interior to the middle line in Figure 20a is what is referred to as the "cocoon" throughout this paper. The shocked ambient gas lies between the bow shock and the cocoon and is not discussed further in this paper. The jet is identified in the simulations by means of trace particles which are injected together with the jet gas.

Slices are taken across the cocoon, and the average pressure within the cocoon is computed for each slice as described above. This average pressure is plotted as a function of distance from the hot spot in Figure 20b, and is normalized to be unity at the location of the hot spot. This measure of the pressure includes only the thermal pressure of the "gas" within the cocoon of the numerical simulation and does not include kinetic pressure. In the numerical simulation, the average pressure in slices across the cocoon undergo a series of oscillations as we move along the symmetry axis of the bridge.

The lateral expansion of the cocoon (i.e., as defined by the contact discontinuity) and that of the bow shock are shown in Figures 20c and d, and are normalized to be unity at the location of the hot spot. Like the bridge width, and the average pressure in a slice across the bridge (i.e., the cocoon), the lateral expansion speed of the cocoon undergoes a series of oscillations rather than varying smoothly along the contact discontinuity. This variation in lateral expansion speed is reflected in differences in the bridge width. For example, in the simulation the bridge width is seen to have a bulge at distances from the hot spot of about 10 to 30 kpc, and this corresponds to a region where there is an increase in the lateral expansion speed of the cocoon relative to nearby points. The lateral expansion speed of the bow shock varies much more smoothly and monotonically with distance from the hot spot. And, appears to generally follow $U_b \propto D^{1/2}$, which is predicted theoretically for the regions in which the expansion speed exceeds the ambient sound speed, after which the expansion speed is expected to level off (e.g., Begelman & Cioffi 1989; Daly 1990, 1994; Wellman et al. 1997a; Reynolds, Heinz, & Begelman 2002; Carvalho & O'Dea 2002a).

3.2. Dynamical and Synchrotron Age

The ratio between the source advance speed and the initial jet speed is shown in Fig. 21 as a function of source size. For comparison, we also show the ambient sound speed (dashed line). We see how the source decelerates rapidly with its Mach number relative to the ambient sound speed decreasing by a factor of ~ 22 from ~ 70 to ~ 3.2. This is due to the progressive increase of the jet head radius. The observed speed fluctuations are also due to oscillations of the head radius. These oscillations of the head radius are probably driven by vortex shedding (e.g., Lind et al 1989; Norman, Winkler, & Smarr 1982). We note that changes in jet momentum flux may also drive changes in the advance speed. Near the end of the simulation, an increase is observed in the advance speed which experience indicates is a transient phenomenon.

Two effects likely to occur in nature that are not included in the simulation may also come into play. In nature, the density of the ambient gas may be slowly decreasing with distance from the central engine rather than remaining constant, and this would cause the decline in the head velocity to be less significant. On the other hand, in nature the outflow axis of the jet may "wobble" rather than pointing in a fixed direction (as in the simulation), which would go in the opposite sense, and at any given time would cause the velocity of the head to be lower (e.g. Scheuer 1982; Cox, Gull, & Scheuer 1991). This second effect could also modify the bridge width as a function of distance from the hot spot.

The dynamical age of Cygnus A determined using the ram pressure of the hotspot is about an order of magnitude larger than the estimated synchrotron age (Carilli et al. 1991). It has been suggested by some authors that this discrepancy can be alleviated if one relaxes the equipartition hypothesis when estimating the magnetic field. According to Carilli et al. the magnetic field must be 1/3 of the equipartition value. Similar results have been found by Perley and Taylor (1991) for 3C295, and by Wellman, Daly and Wan (1997a,b) for a large sample of sources. The deceleration of the source head observed in the simulations can, at least in part, be responsible for the discrepancy.

Thus, the age calculated using the speed at the source maximum length is larger than the real age of the source. In our simulation the difference is not too large because at the end of the simulation the head speed has momentarily increased. However, if we calculate the age by taking the head speed when the source was, for instance, ~ 51 kpc in size, it would be larger than the real age by a factor ~ 2. Thus, this effect can account for only a part of the discrepancy between the ram-pressure balance and synchrotron ages found by Carilli et al. (1991).

3.3. Surface Brightness and Radio Emissivity

We have calculated the volume emissivity of the source assuming that the energy density of the relativistic electron component is proportional to the hydrodynamical (thermal) pressure of the gas inside the cocoon and an equipartition magnetic field. This is easy to do since the radio emissivity is proportional to $P^{7/4}$, as described at the end of §2.4. We will also consider separately contributions proportional to the thermal pressure, the kinetic pressure, and the total pressure (see Figure 25). We assume that the radio emission comes from the jet itself and the cocoon (Leahy, 1991) where the pressure is higher than ambient pressure. This region (corresponding to the region interior to the middle line in Figure 20a) is filled with jet material which has been shocked in the head and expands laterally. Besides any non-relativistic gas that may be present in this region, it is assumed that the region also contains the basic ingredients necessary to generate synchrotron emission, that is, a mixture of magnetic field and relativistic electrons most probably accelerated by Fermi process at the strong shock region in the jet head. We integrated the radio emissivity along the line of sight (assuming the source lies in the plane of the sky) to obtain the surface brightness, which allows us to draw synthetic radio images of the source. We have also taken into account radiation loss of the relativistic electron population in a very simple way. We divided the cocoon into slices and assigned an age to each slice equal to the time that has passed since it has been laid down by the advancing jet head. The modified spectrum is then calculated using the Kardashev-Pacholczyk model (Kardashev 1962; Pacholczyk 1970) supposing that the magnetic field is the equipartition field.

In this manner, we were able to predict the radio structure that would be observed from the source indicated by the numerical simulation. In Fig. 22 we show the predicted 151 MHz radio image of the source at five evolutionary stages; the synthetic data have been smoothed by a Gaussian with FWHM of 3 arcsec to match the 151 MHz data, as shown by the black circle in panel e of the figure. The age of the source corresponding to each panel is: (a) 1.35 Myr, (b) 4.53 Myr, (c) 6.17 Myr, (d) 8.89 Myr and (e) 9.15 Myr. One can clearly see the characteristic edge-brightened shape of powerful FR-II sources and an aspect ratio resembling that of Cygnus A. When the source is young, radiative energy losses are negligible and we can see the radio bridge extending all the way from the head to the central galaxy (panels b and c). As the source ages, the central parts becomes less luminous and it assumes the classical double lobe shape (panel e). The hotspots are evident in all the simulated images.

Cross-sectional slices of the surface brightness distribution for the source as it appears in panel e, when it is about 9 Myr old, are shown in Fig. 23. The second panel in the first row corresponds to the position of the hotspot while the bottom ones show the parts of the

source near the central object. We have normalized the surface brightness to unity at the hot spot and the scale in each row is the same as that in Fig. 4 at 151 MHz. The simulated surface brightness is qualitatively similar to that observed in Cygnus A (Figs. 2, 3, 4, 5). Of course, the simulation is axisymmetric and thus so are the cross-sectional surface brightness slices, whereas in nature this is not always the case.

The Gaussian fit is shown as a dotted line in the figure. The central spikes that appear in some of the panels are caused by the jet contribution to the surface brightness. The spikes are more evident in those regions of the jet where it has been compressed (Fig. 19). The Gaussian fits provide a reasonable approximation to the actual surface brightness slices over most of the source except along row 3 where the wings of the Gaussian fit clearly extend well beyond the boundary of the source.

Fig. 24 shows the predicted average surface brightness of a slice as a function of distance from the hotspot in the numerical simulation; the average surface brightness is obtained as described in section 2.3, but using the true width of the simulated source.

Here we investigate how the different forms of energy (thermal pressure, kinetic pressure, and total pressure) could contribute to the radio emission. Again, the pressure in relativistic electrons and magnetic fields is assumed to be proportional to the gas pressure, this being determined by the local thermal pressure, kinetic pressure, or total pressure given by the numerical simulation. The thermal pressure is the thermodynamic pressure associated with the gas microscopic motion (discussed in §3.1). The kinetic pressure is equal to $(\Gamma - 1)$ times the kinetic energy density, where the kinetic energy density $0.5\rho v^2$ depends on the large-scale, macroscopic or bulk velocity v of the gas. The total pressure is the sum of the thermal and kinetic pressures. We also use the approximation that the emissivity is proportional to $P^{7/4}$ (described in §2.4). Considering the kinetic pressure allows for the fact that macroscopic kinetic energy in the form of turbulent motion could be transferred to the relativistic component through the Fermi process or through hydromagnetic instabilities (e.g. De Young 1980; Eilek & Henriksen 1984; Eilek & Shore 1989). For this figure, the radio emissivity is calculated supposing that the local pressure of the relativistic fluid, including the relativistic electrons and magnetic fields, is equal to the total pressure (full line), thermal pressure (dashed-dotted line) and the kinetic pressure (dotted line).

We observe that in many places the contribution of the kinetic pressure can be very important. This is a feature that is not being considered by the majority of works in the literature. It is very interesting to note that the surface brightness profile indicated by the total pressure (kinetic plus thermal) is very similar to that of the 151MHz data (see Figure 11). The surface brightness profile indicated by the thermal pressure alone is very similar to that of the 1345 MHz data (see Figure 11). This suggests that different forms of energy

within the bridge may enhance radio emission at different frequencies differently. It is easy to see how this could occur since the radio emission at different frequencies is produced by relativistic electrons with different Lorentz factors. Thus, it would only require that the thermal pressure produces an underlying relativistic electron population with a power law distribution at all Lorentz factors, while the kinetic pressure boosts additional relativistic electrons to Lorentz factors that produce the 151 MHz emission but not the 1345 MHz emission. For example, through hydromagnetic processes the kinetic pressure could boost relativistic electrons with lower Lorentz factor up to the Lorentz factors needed to produce 151 MHz emission. This could help to explain some of the changes in the radio spectrum seen across the source.

To investigate this further, we compare the average thermal pressure, and the total average pressure (thermal plus kinetic pressures) obtained from the numerical simulation with the average pressure obtained from the 151 MHz and 1345 MHz data (Figure 25). To do this, the physical value of the units on the pressure obtained from the simulation were investigated, and were determined to be $1.596 \times 10^{-8} n_a$ dyn/cm^2, where n_a is the ambient gas density. A value of $n_a = 10^{-2}$ cm^{-3} was adopted since this is consistent with X-ray measurements of the gas in the vicinity of the radio source (e.g., Smith et al. 2002). The behavior of the pressures in the simulations roughly tracks that seen in the data. Of course, it is possible that the value of b in the hot spot region is closer to unity (e.g., Hardcastle et al. 2004; Donahue, Daly, & Horner 2003; Hardcastle et al. 2002; Wilson, Young, & Shopbell 2000), while that in the bridge is ~ 0.25. (e.g., Carilli et al. 1991; Perley & Taylor 1991; Wellman et al. 1997b). The value of b does not affect the pressures determined using the numerical code (which only depend on the scaling factor n_a), but it does affect the pressure determined from the data. If b in the hot spot in closer to unity, then the pressure determined using the data will be lower in this region that the values shown. This would improve the fit to the 1345 MHz data, and worsen the match with the 151 MHz data. Another effect to consider is the efficiency factor (converting gas kinetic into relativistic energy) used in converting surface brightness into pressure, which could vary with location within the source or could have an energy dependence, resulting in a frequency dependence. In addition, consider particle re-acceleration within the bridge region or a backflow could be important in the source. In view of these factors, the rough overall agreement between the data and the simulation is encouraging.

Finally, in Fig. 26 we compare the thermal pressure determined from the simulation at several different times with that estimated from the 151 MHz empirical data for the two sides of Cygnus A, each normalized to match at the peak of the hot spot. Sources are dynamic, constantly changing with time, so we consider snapshot corresponding to panels c, d, and e of Figure 24 re-scaled to have a length of 60 kpc. The dynamic nature of the source is obvious

from these snapshots. The agreement is better than for the surface brightness distribution and this is due to the fact that the simulated pressure profile does not depend upon the bridge width. As we shall see below, the simulated and observed width do not agree equally well over the entire bridge extent. We see that the pressure profile varies considerably with time over the course of the simulation. This implies that there is no "steady-state" pressure distribution in the lobes.

3.4. Bridge Width

We compare the "true" width of the bridge in the simulation (Figure 20a) with the FWHM and second moment of the synthetic surface brightness distribution (Figure 27), where only the thermal component of the surface brightness was considered. We find that while the second moment gives a good fit to the true cocoon width, the Gaussian FWHM deviates significantly. (Note: this is not seen in the data, where the second moment and FWHM of the Gaussian fits track each other quite well Figure 10). The main departure in the simulation occurs between 20 and 30 kpc from the hot spot. This can be attributed to the fact that the cross-sectional slices of the surface brightness distribution in this region exhibits a double peak as can be seen in Fig. 23. This double peak implies that the gas pressure distribution inside the simulated cocoon is higher near its edges, at least in the region in question ($20 - 30$ kpc).

The ratio $\zeta = W_G/W_2$ between the two quantities is in the range $\sim 1.2 - 1.8$ with an average value 1.39 ± 0.07. For a perfect Gaussian distribution, the ratio $\zeta = \sqrt{2 \ln 2} \simeq 1.177$. To compare this with the empirical data shown in Fig. 10 we note that in this figure we have plotted $2\zeta = W_G/(\text{second moment})$. Since the value of the empirical data is in the range $2 - 3$ we conclude that the results of the simulations $2\zeta \sim 2.4 - 3.6$ are in fair agreement with the data.

Figure 4 shows a comparison between the observed FWHM of the radio source with the "true" width of the simulated source. We see that the simulation shows the same general behavior as the radio source.

3.4.1. Emissivity Distribution

As mentioned above, the value of ratio $\zeta = W_G/W_2$ will depend on the emissivity distribution across the cocoon. In this sense, the ratio may be used as a diagnostic of the distribution of emissivity.

We have thus investigated this by calculating the ratio ζ for a simple model cocoon whose radius varies smoothly according to

$$R_c = 0.5 + 9.5 \left(\frac{D}{60kpc} \right)^{1/2}$$

where D is the distance from the hot spot and R_c is in kpc. We studied five cases with different pressure profiles $P(r)$. The radial dependence of P is shown in Table 1. In all cases $P = 0$ for $r > R_c$.

We calculated the surface brightness using the same beam size as the empirical data and calculated the second moment and fit a Gaussian to the surface brightness profile perpendicular to the cylinder axis in order to determine the ratio ζ. The values of W, W_G and W_2 for four of the model bridges in Table 1 are shown in Fig. 29. We can clearly see how the relation between the true width W and the calculated ones W_G and W_2 depends strongly on the pressure distribution across the cocoon.

In Table 1 we show the average values of the Gaussian width, the second moment and ζ for the five distributions. We see that for Model A both the Gaussian fit and the second moment are about 55% to 70% of the true width, and thus need to be normalized to be used as a direct measure of the bridge width. For the other models the Gaussian width increasingly departs from the true width as the peak of pressure distribution moves away from the source axis. On the other hand, the second moment gives a better estimate when the pressure distribution concentrates near the border of the cocoon.

We notice that the range of values of the ratio ζ of the Gaussian FWHM and the second moment width W_2 for the five distributions is in agreement with the value from the numerical simulations ($1.2-1.8$). The average value observed in Cygnus A ($\sim 2.5 = 2 \times 1.25$) is compatible with an emissivity distribution concentrated near the source axis (Model A). In a few cases when it reaches higher values ($\sim 3 = 2 \times 1.5$), the pressure distribution in these regions must have two separate peaks as in Model E. In fact, if we look at the deconvolved emissivity distribution of Cygnus A at 151 MHz (Figs. 15, 16, 17, 18) we see that this seems indeed to be the case in several sections of the bridge. Thus, the ratio between the Gaussian width and the second moment can provide a diagnostic of the emissivity profile in the lobe. It may be necessary to run 3-D numerical simulations to properly "calibrate" this diagnostic ratio.

We have seen that, for the numerical simulation, the second moment of the surface brightness distribution gives a more stable estimate of the bridge width in our model cocoon than the Gaussian fit (e.g., Fig. 27). If this applies to real sources it can be used as a measure of its real width, provided we have a proper normalization factor. Our simulation

gives an average value for the ratio between the cocoon and Gaussian width $\beta_G = W/W_G$ of $\beta_G = 0.91 \pm 0.12$; while the average ratio of the true width to the second moment $\beta_2 = W/W_2$ is $\beta_2 = 1.26 \pm 0.04$.

We note that (using $\zeta = W_G/W_2$ as a diagnostic, Table 1) the range of values of ζ found in Cygnus A indicates that, at least in some regions, the bridge contains high pressure edges. Carilli et al. (1991) suggest that an edge brightening of the lobes could account for the increase in the magnetic field from the center to the edge of the lobes needed to explain the estimated age gradient. If this is the case, the Gaussian fit overestimates the bridge width as in Models D and E (Table 1) and, again, the second moment should be used to calculate the bridge width.

4. SUMMARY

We present a comparison of radio observations of the archetypal powerful radio galaxy Cygnus A and 2-D numerical hydrodynamical simulations. We characterize some global trends in the observed radio properties and compare them with the properties of a simulated radio source. We have analyzed detailed radio images at 151 MHz (Leahy et al. 1989) and 1345 MHz (Carilli et al. 1991). We have determined the surface brightness, emissivity, Gaussian FWHM, first and second moment of cross-sectional slices of the source as a function of distance along the bridges. We have also estimated the average pressure and minimum energy magnetic field in the radio plasma as a function of distance along the bridges. We find the following trends in global properties.

- The first moment of the brightness distribution perpendicular to the source axis is a measure of the surface brightness weighted center of the source. We find that the first moment wanders with a peak-to-peak amplitude of ~ 10 arcsec. The sense of the wander has the opposite sign on the two sides of the source, but there is not an exact correspondence.

- The width of the surface brightness distribution perpendicular to the source axis can be well characterized by a Gaussian over most of the length of the source. The ratio of the Gaussian FWHM to the second moment is fairly constant along the source with an average value of about 2.5 indicating that they give roughly consistent measurements of the source width. The radio lobe increases in width with distance from the hot spot. Superimposed on this general expansion are several "wiggles."

- The average surface brightness, estimated pressure, and estimated minimum energy B field decrease with distance from the hot spots.

- We find evidence for significant structure in the estimated cross-sectional slices of emissivity.

Following the methods of Carvalho & O'Dea (2002a,b) we present the results of 2-D numerical hydrodynamical simulations of light (density contrast $\zeta = 10^{-4}$), supersonic (jet Mach number $M = 10$) jets propagating in a constant density environment. The results from the simulations are the following.

- Jets propagating in a constant density atmosphere will decelerate with time (see also Carvalho & O'Dea 2002a). Thus, the estimated dynamical age of the source will be greater than the actual age of the source. For a source similar to Cygnus A the difference will be about a factor of 2.

- We have run the simulations with several different grid widths. In the largest grid, the entire source is contained on the grid, while in the smaller grids, the bow shock eventually leaves the grid laterally. We find that the details of the cocoon properties differ in these simulations, though the overall properties of the cocoons are similar.

- The pressure profile varies considerably with time over the course of the simulation. This implies that there is no "steady-state" pressure distribution in the lobes. There is considerable time dependence in the variation of the average surface brightness in the lobe near the hot spots, possibly due to vortex shedding.

- The kinetic pressure in the cocoon (due to large scale turbulence) can make a significant contribution to the total pressure of the cocoon. We speculate that the thermal pressure produces an underlying relativistic electron population with a power law distribution at all Lorentz factors, while the kinetic pressure adds "extra" relativistic electrons with the Lorentz factors that produce the 151 MHz emission and not the 1345 MHz emission. For example, through hydromagnetic processes the kinetic pressure could boost relativistic electrons with lower Lorentz factor up to the Lorentz factors needed to produce 151 MHz emission. This could help to explain some of the changes in the radio spectrum seen across the source.

- The second moment gives an accurate representation of the "true" width of the simulated source. The Gaussian FWHM tends to be about 40% larger than the true width and can be systematically in error if the surface brightness exhibits multiple peaks. We suggest that the ratio of the Gaussian FWHM to the second moment may be a diagnostic of the emissivity profile in the lobes. However, "calibration" of this diagnostic probably requires 3-D simulations. Applying this diagnostic reveals that

bridge contains high pressure edges. This is consistent with the suggestion of Carilli et al. (1991) that an edge brightening of the lobes could account for the increase in the magnetic field from the center to the edge of the lobes needed to explain the estimated age gradient.

We compare our simulations with the properties of the observed radio sources in two complementary ways. We note that the pressure is directly determined in the simulation but is estimated from the radio data, while the surface brightness is directly determined from the radio data but is estimated from the simulations.

The simulations can qualitatively reproduce the overall observed morphology and the behavior of the cross-sections in surface brightness, the decline in surface brightness with distance from the hot spots, and the width of the lobes. This suggests that the 2-D simulations give a reasonable representation of the properties of Cygnus A.

This is especially encouraging given that the outflow axis of the jets in Cygnus A may wobble while those in the numerical simulation are held steady, and given that the ambient gas density in the simulation is assumed to be constant. The good agreement between the simulation and the data suggest that these effects are relatively small for a source like Cygnus A.

We are grateful to Paddy Leahy and Chris Carilli for sending us their radio data and to the referee for a thoughtful review of the manuscript. JCC acknowledges the financial support of PRONEX/Finep and CNPq and the hospitality of STScI where this work was carried out. This work was supported in part by a grant to C. O'Dea from the STScI Collaborative Visitor Program which funded visits by JCC to STScI, and by grant AST-0206002 to R. Daly from the U. S. National Science Foundation.

REFERENCES

Alexander, P., & Leahy, P., 1987, MNRAS, 225, 1

Alexander, P., & Pooley, G. G. 1996, in Cygnus A - Study of a Radio Galaxy, eds. C. L. Carilli & D. E. Harris, (Cambridge University Press, Cambridge), p. 149

Begelman, M. C., & Cioffi, D. F. 1989, ApJ, 345, L21

Carilli, C. L., Perley, R. A., Dreher, J. W., & Leahy, J. P., 1991, ApJ, 383, 554

Carvalho, J. C., & O'Dea, C. P., 2002a, ApJS, 141, 337

Carvalho, J. C., & O'Dea, C. P., 2002b, ApJS, 141, 371

Cioffi, D. F., & Blondin, J. M. 1992, ApJ, 392, 458

Clarke, D. A., Norman, M. L. & Burns, J. O. 1989, ApJ, 342, 700

Cox, C. I., Gull, S. F., & Scheuer, P. A. G. 1991, MNRAS, 252, 558

Daly, R. A. 1990, ApJ, 355, 416

Daly, R. A. 1994, ApJ, 426, 38

De Young, D. S. 1980, ApJ, 241, 81

Donahue, M., Daly, R. A., & Horner, D. J. 2003, ApJ, 584, 643

Eilek, J. A, & Henriksen, R. N. 1984, ApJ, 277, 820

Eilek, J. A., & Shore, S. N. 1989, ApJ, 342, 187

Falle, S. A. E. G. 1991, MNRAS, 250, 581

Hardcastle, M. J., Birkinshaw, M, Cameron, R. A., Harris, D. E., Looney, L. W., & Worrall, D. M. 2002, ApJ, 581, 948

Hardcastle, M. J., Harris, D. E., Worrall, D. M., & Birkinshaw, M. 2004, ApJ, in press (astro-ph/0405516)

Hardee, P. E., & Norman, M. L. 1990, ApJ, 365, 134

Kardashev, N. S., 1962, Soviet-AJ, 6, 3171

Komissarov, S. S., & Falle, S. A. E. G. 1997, MNRAS, 288, 833

Komissarov, S. S., & Falle, S. A. E. G. 1998, MNRAS, 297, 1087

Krause, M. 2003, A&A, 398, 113

Leahy, J. P. 1991, In Beams and Jets in Astrophysics, ed. P. A. Hughes, (Cambridge University Press), 100

Leahy, J. P., Muxlow, T. W. B., & Stephens, P. W. 1989, MNRAS, 239, 401

Lind K.R., Payne D.G., Meier D.L., & Blandford R.D. 1989, ApJ, 344, 89

Loken, C., Burns, J. O., Clarke, D. A., & Norman, M. L. 1992, ApJ, 392, 54

Marti, J. M^a., Müller, E., Font, J. A., Ibanez, J. M^a., & Marquina, A. 1997, ApJ, 479, 151

Mioduszewski, A. J., Hughes, P. A., & Duncan, G. C. 1997, ApJ, 476, 649

Norman, M. L., Smarr, L., Winkler, K.-H., A., & Smith, M. D., 1982, A&A, 113, 285

Pacholczyk, A. G., 1970, Radio Astrophysics (San Francisco: Freeman)

Perley, R. A, & Taylor, G. B., 1991, AJ, 101, 1623

Reynolds, C. S., Heinz, S., & Begelman, M. C., 2002, MNRAS, 332, 271

Rosen, A., Hughes, P. A., Duncan, G. C., & Hardee, P. E. 1999, ApJ, 516, 729

Scheuer, P. A. G. 1982, in: Extragalactic Radio Sources, IAU Symposium No. 97, eds. D. S. Heeschen & C. M. Wade (D. Reidel), p. 163

Smith, D. A., Wilson, A. S., Arnaud, K. A., Terashima, Y, & Young, A. J. 2002, ApJ, 565, 195

Wan, L., Daly, R.A., & Guerra, E. J., 2000, ApJ, 544, 671

Wellman, G.F., Daly, R.A., & Wan, L. 1997a, ApJ, 480, 79.

Wellman, G.F., Daly, R.A., & Wan, L. 1997b, ApJ, 480, 96.

Wilson, A. S., Young, A. J., & Shopbell, P. L. 2000, ApJ, 544, 27

This preprint was prepared with the AAS LaTeX macros v5.2.

Table 1. Comparison between calculated and true width for a model bridge

	Pressure distribution $P(r)$	Gaussian fit $< W_G/2R_c >$	Second moment $< W_2/2R_c >$	$< \zeta = W_G/W_2 >$
A	$1 - \frac{r}{R_c}$	0.673	0.550	1.223
B	1	1.075	0.786	1.367
C	$\left(\frac{r}{R_c}\right)^{1/2}$	1.211	0.848	1.428
D	$\left(\frac{r}{R_c}\right)^{1}$	1.301	0.889	1.463
E	$\left(\frac{r}{R_c}\right)^{2}$	1.416	0.939	1.507

Fig. 1.— Examples of cross-sectional slices used to define the surface brightness profiles shown in Fig. 2 for the 151 MHz data (left) and the 1345 MHz data (right). The distance of the slice from the hot spot is indicated at the bottom on the slice. The images have been rotated slightly for ease of display and the left side is the south-east lobe and the right side is the north-west lobe.

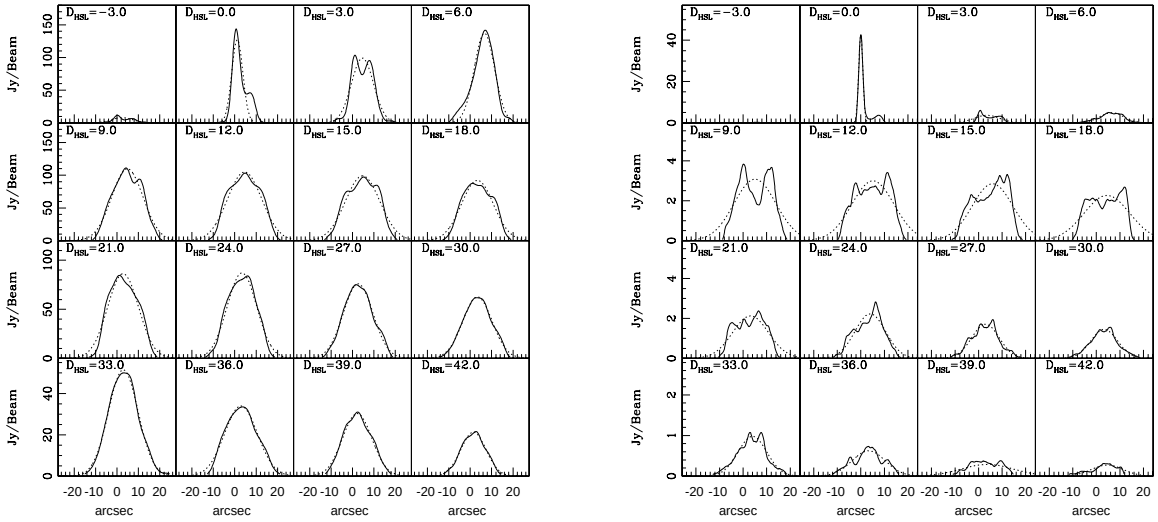


Fig. 2.— Cross-sectional surface brightness profiles (solid lines) and Gaussian fits (dashed lines) for the Left side of Cygnus A at 151 MHz (left panel) and 1345 MHz (right panel). The distance of the slice from the hot spot is indicated for each slice.

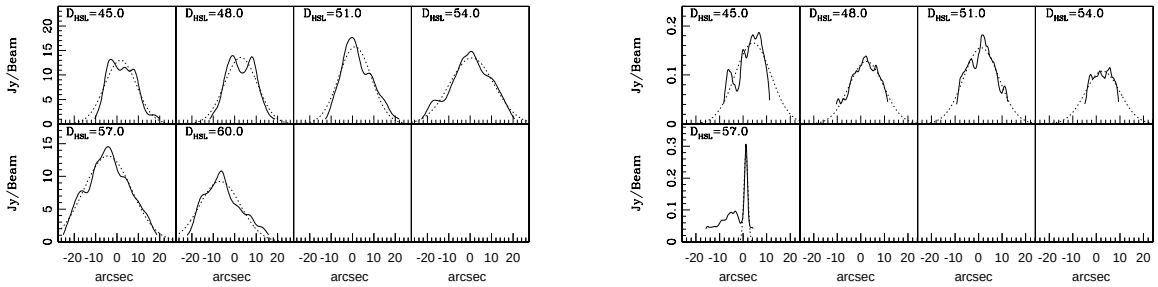


Fig. 3.— Continuation of the cross-sectional surface brightness profiles and Gaussian fits for the Left side of Cygnus A at 151 MHz (left panel) and 1345 MHz (right panel).

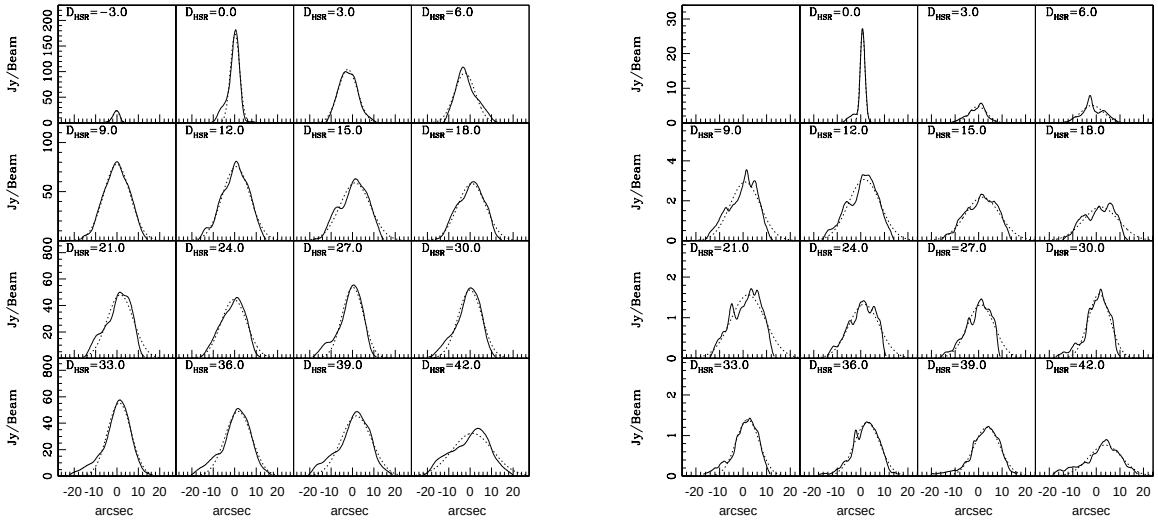


Fig. 4.— Cross-sectional surface brightness profiles (solid lines) and Gaussian fits (dashed lines) for the Right side of Cygnus A at 151 MHz (left panel) and 1345 MHz (right panel). The distance of the slice from the hot spot is indicated for each slice.

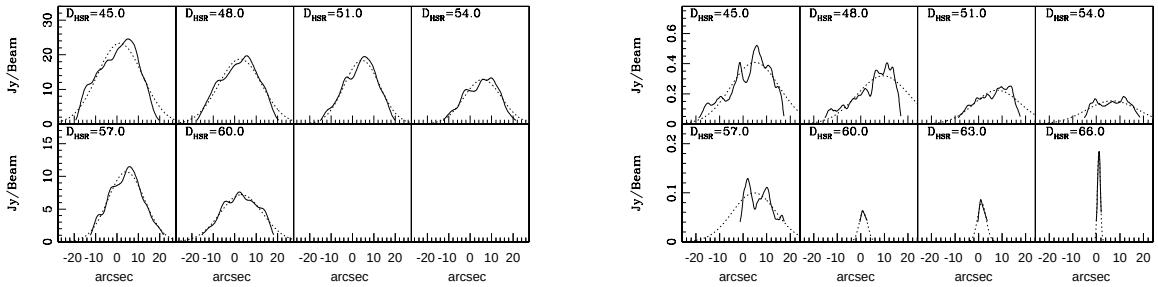


Fig. 5.— Continuation of the cross-sectional surface brightness profiles and Gaussian fits for the Right side of Cygnus A at 151 MHz (left panel) and 1345 MHz (right panel).

Fig. 6.— The full width at half max of the best fit Gaussian as a function of slice distance from the hot spot at 151 MHz (left panel) and 1345 MHz (right panel). The upper panels show results from the Left side of the source, while the lower panels show results from the Right side.

Fig. 7.— Ratio of the FWHM obtained at 151 MHz to that obtained at 1345 MHz. A more narrowly focused view is shown on the right panel.

Fig. 8.— The first moment of the cross-sectional surface brightness profiles as a function of distance from the hot spot. The 151 MHz data is shown on the left panels, while the 1345 MHz data is shown on the right panels; the Left side of the source is shown in the upper panels, and the Right side is shown in the lower panels.

Fig. 9.— The second moment of the cross-sectional surface brightness profiles as a function of distance from the hot spot for the 151 MHz data (left panel) and the 1345 MHz data (right panel). The upper panels show results from the Left side of the source and the lower panels show results from the Right side of the source.

Fig. 10.— The ratio of the Gaussian FWHM to the second moment as a function of distance from the hotspot for the 151 MHz data (left panel) and the 1345 MHz data (right panel). Measurements from the left side of the source are shown in the upper panels; the average values of these are 2.59 ± 0.07 and 2.45 ± 0.03 for the 151 and 1345 MHz data respectively. Measurements from the right side are shown in the lower panels; the average values are 2.49 ± 0.07 and 2.53 ± 0.03 for the 151 and 1345 MHz data respectively.

Fig. 11.— The average surface brightness in a cross-sectional surface brightness slice as a function of distance from the hot spot for the 151 MHz data (left panel) and the 1345 MHz data (right panel) obtained assuming the diameter of the bridge at each distance from the hot spot can be approximated by the FWHM of the best fit Gaussian. Results from the Left side of the source are shown in the upper panels, while those from the Right are shown in the lower panels.

Fig. 12.— The average pressure in a cross-sectional surface brightness slice as a function of distance from the hot spot for the 151 MHz data (left) and the 1345 MHz data (right). The pressure for the 151 MHz data has units of 1.2×10^{-11} erg cm$^{-3}(1.33b^{-1.5} + b^2)$, where b parameterizes the offset from minimum energy conditions. For minimum energy conditions, $b = 1$, and the normalization factor or pressure unit for the 151 MHz data is 2.8×10^{-11} erg cm^{-3}, while for a field strength that is about 0.25 the minimum energy value, the normalization is 1.3×10^{-10} erg cm^{-3}. The normalization factor for the 1345 MHz data is 10^{-10} erg cm$^{-3}(1.33b^{-1.5}+b^2)$. For minimum energy conditions the pressure unit for the 1345 MHz data is 2.4×10^{-10} erg cm^{-3}, while for $b = 0.25$, the pressure unit is 1.1×10^{-9} erg cm^{-3}. Measurements from the Left side of the source are shown in the upper panels, while those from the Right side are shown in the lower panels.

Fig. 13.— The average minimum energy magnetic field strength in a cross-sectional surface brightness slice as a function of distance from the hot spot for the 151 MHz data (left) and the 1345 MHz data (right). The units of the minimum magnetic field strength for the 151 MHz data are 30 μG, while those for the 1345 MHz data are 88 μG. Estimates from the Left side of the source are shown in the upper panels, while those from the Right side of the source are shown in the lower panels.

Fig. 14.— Method of obtaining the emissivity as a function of radial distance from the slice center.

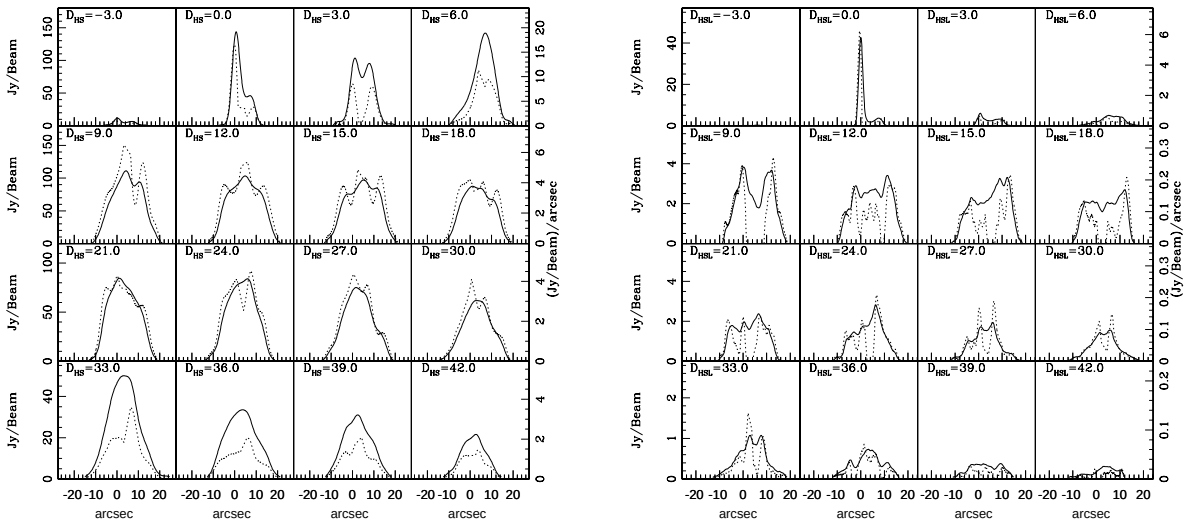


Fig. 15.— The radio emissivities (dashed lines) and cross-sectional surface brightness profiles (solid lines) for the 151 MHz data (left panel) and the 1345 MHz data (right panel) for the Left side of Cygnus A. The units for the 151 MHz data are 1.8×10^{-34} erg s^{-1} cm^{-3} Hz^{-1}, while those for the 1345 MHz data are 9.0×10^{-34} erg s^{-1} cm^{-3} Hz^{-1}.

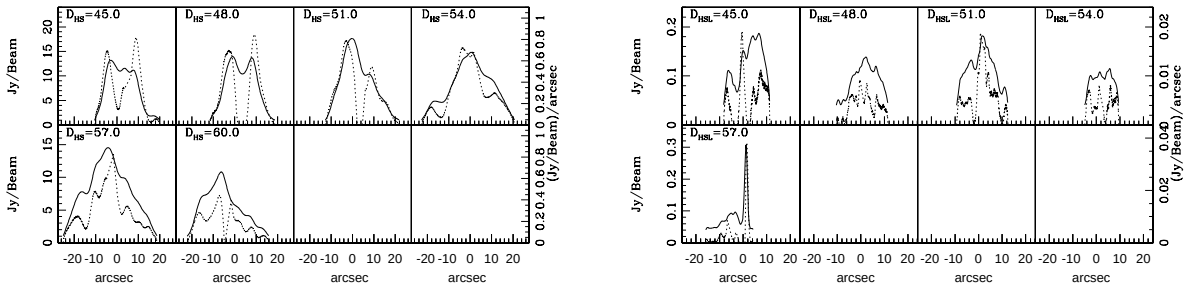


Fig. 16.— Continuation of the radio emissivities and cross-sectional surface brightness profiles for the Left side of Cygnus A.

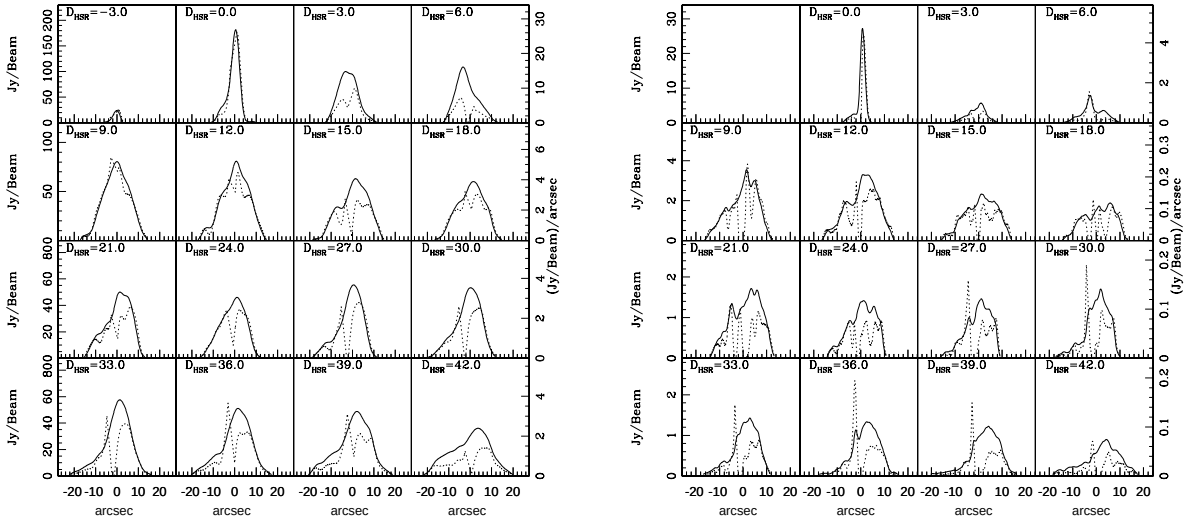


Fig. 17.— The radio emissivities (dashed lines) and cross-sectional surface brightness profiles (solid lines) for the 151 MHz data (left panel) and the 1345 MHz data (right panel) for the Right side of Cygnus A. The units for the 151 MHz data are 1.8×10^{-34} erg s^{-1} cm^{-3} Hz^{-1}, while those for the 1345 MHz data are 9.0×10^{-34} erg s^{-1} cm^{-3} Hz^{-1}.

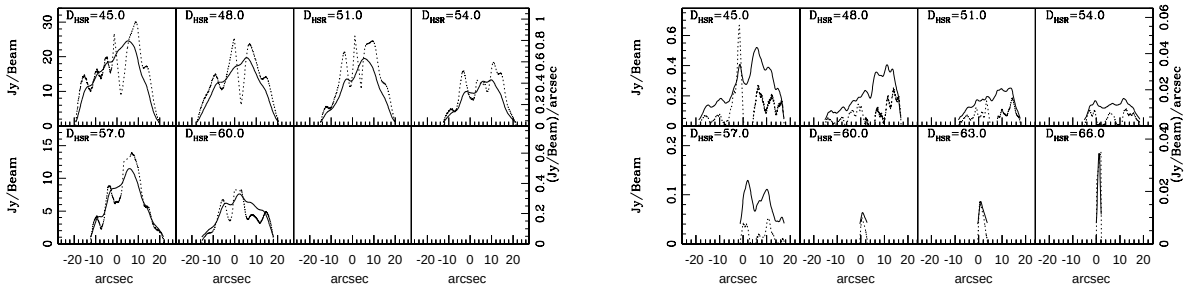


Fig. 18.— Continuation of the and radio emissivities and cross-sectional surface brightness profiles and radio emissivities for the Right side of Cygnus A.

Fig. 19.— Density contour map of a jet propagating in a constant density atmosphere for Run D01 ($M = 10, \eta = 2 \times 10^{-4}$). The grid size is 66 $\times$79 kpc.

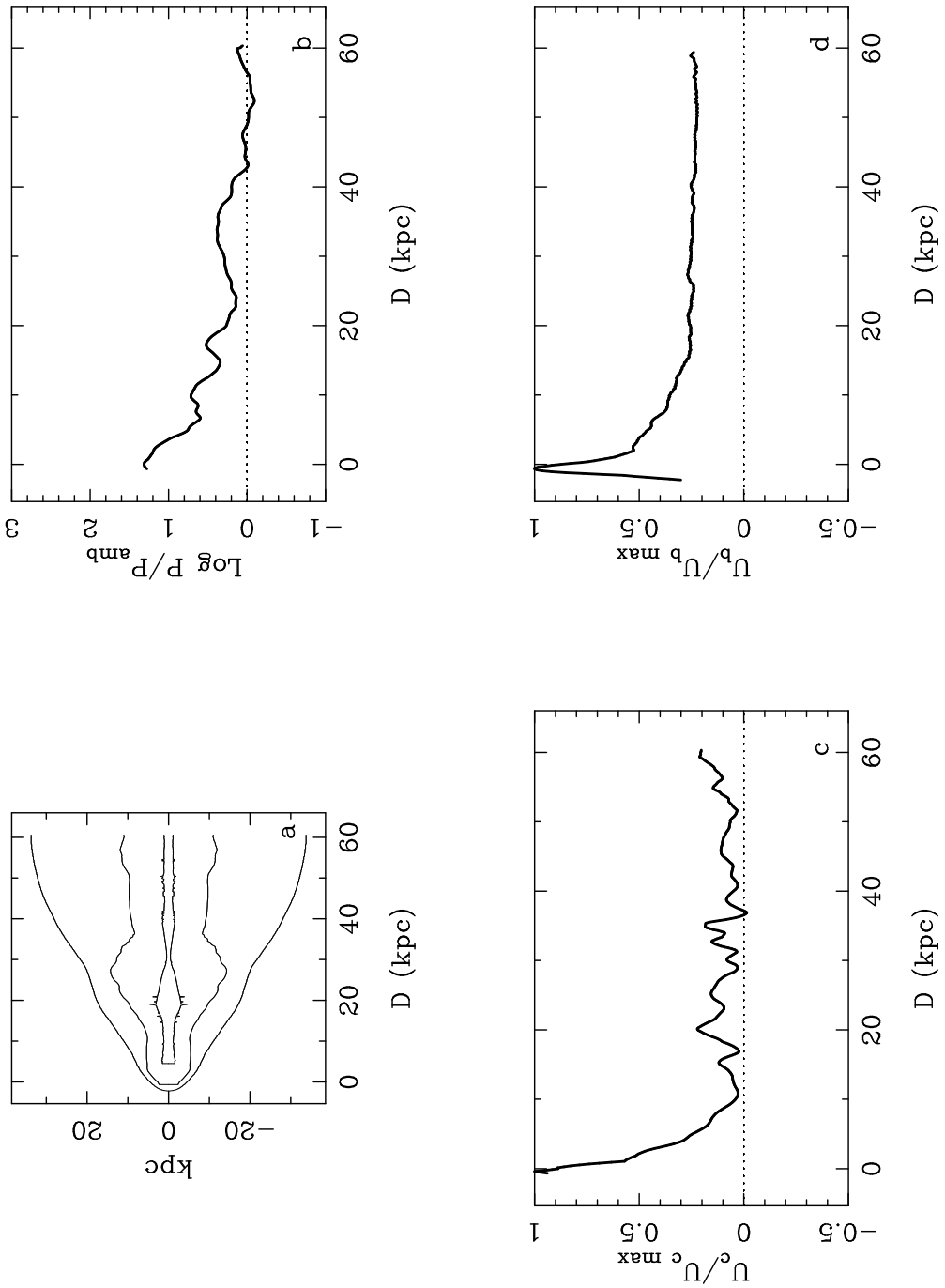


Fig. 20.— (a) Contour of the bow shock, cocoon and jet for the simulation shown in Fig. 19 (Run D01). Panel (b) shows the longitudinal profile of the average cocoon pressure, cocoon lateral speed (c) and bow shock lateral speed (d).

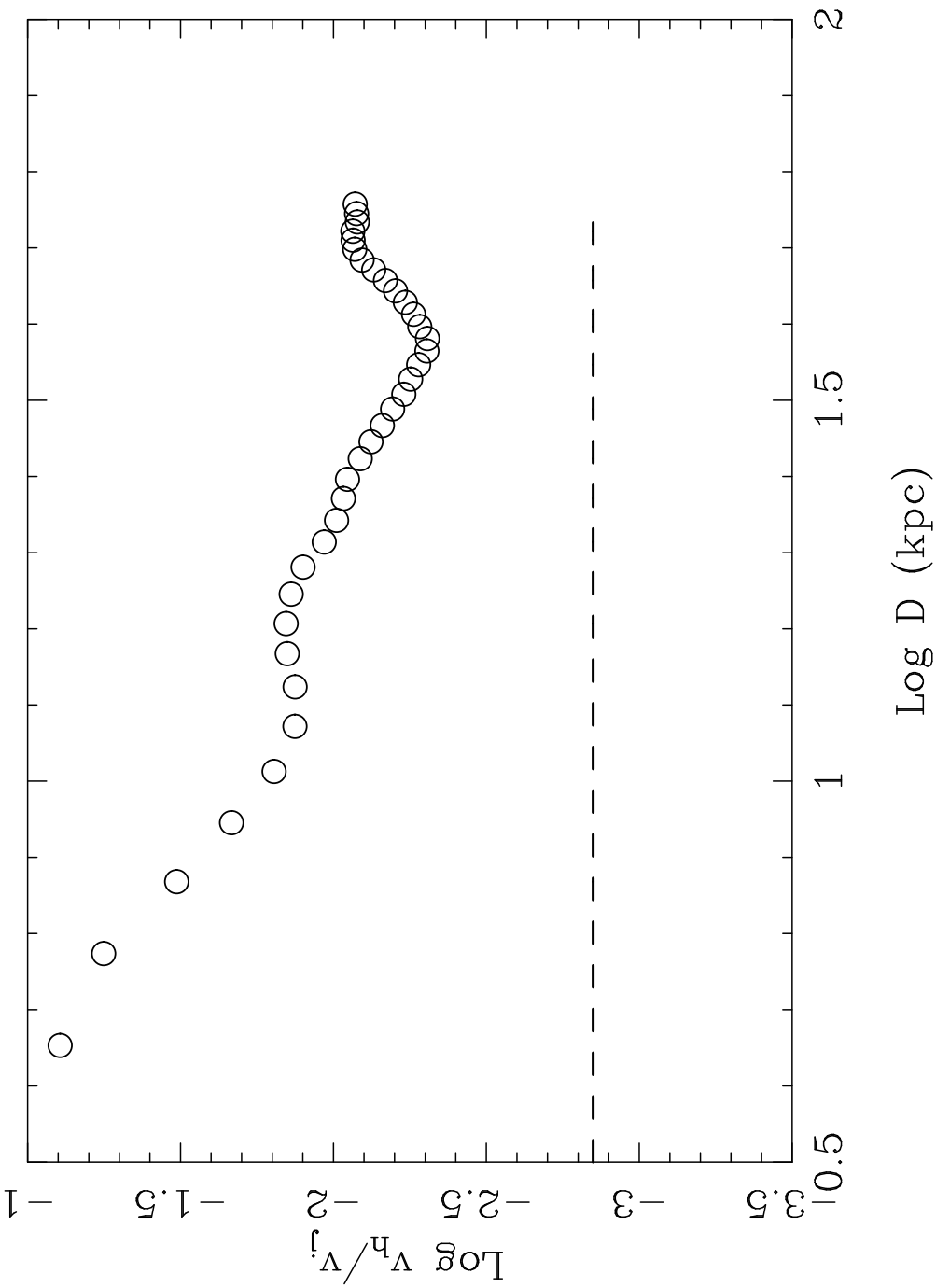


Fig. 21.— Advance speed of the head (open circles) relative to the jet initial speed as a function of source size. The dashed line represents the ambient sound speed.

Fig. 22.— Synthetic radio image showing the time evolution of the numerical simulation of a jet ($M = 10, \eta = 2 \times 10^{-4}$) propagating in a constant density atmosphere. Each panel measures 144 ×54 kpc and the synthetic data have been smoothed by a Gaussian with FWHM of 3 arcsec to match the 151 MHz data, as shown by the black circle in panel e. The age of the source corresponding to each panel is: (a) 1.35 Myr, (b) 4.53 Myr, (c) 6.17 Myr, (d) 8.89 Myr and (e) 9.15 Myr. One can clearly see the characteristic edge-brightened shape of powerful FR-II sources and an aspect ratio resembling that of Cygnus A.

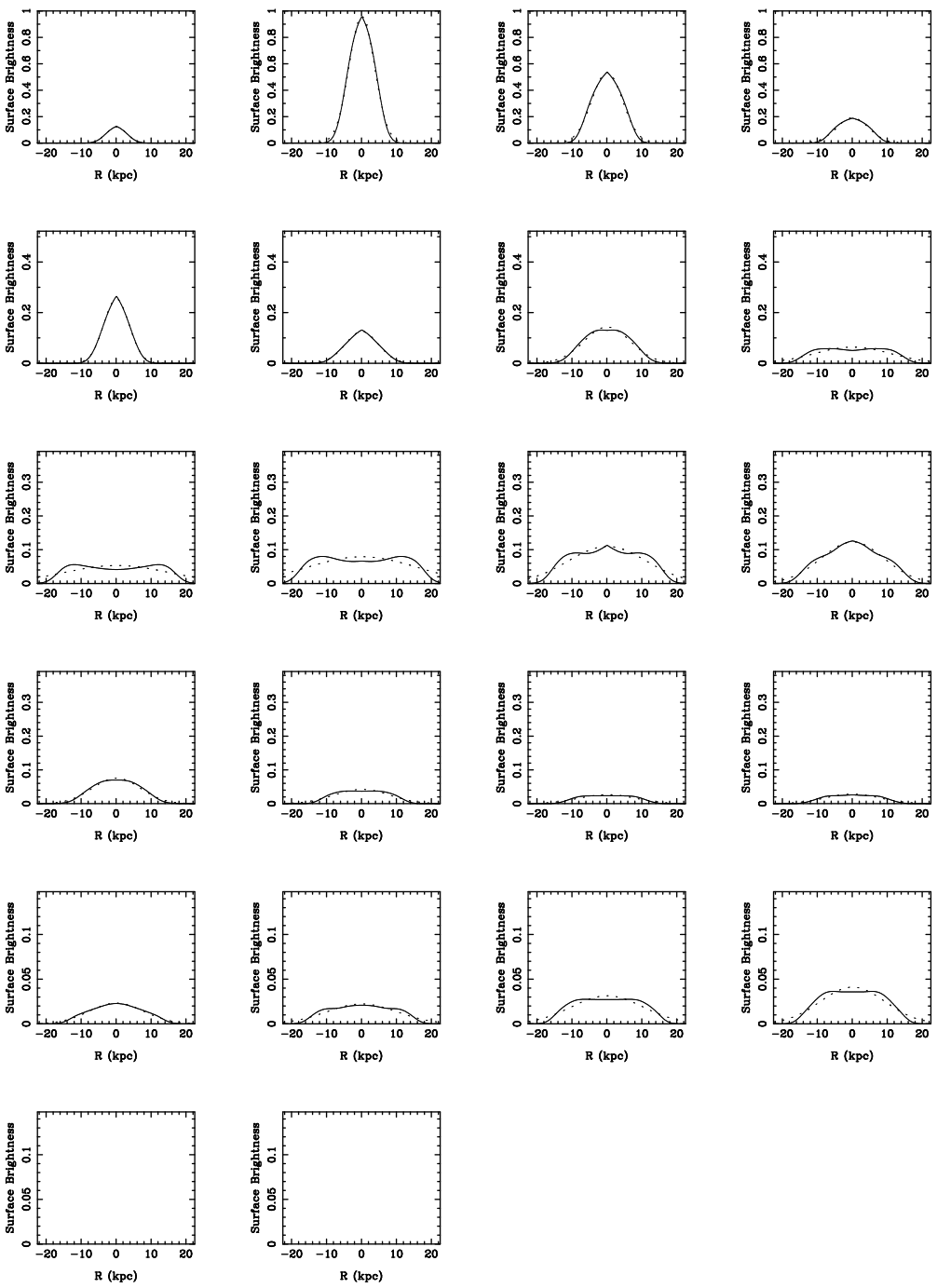


Fig. 23.— Cross-sectional surface brightness profiles (solid lines) and Gaussian fits (dotted lines) for the numerical simulation (Run D01). The distance between each panel is 3 kpc.

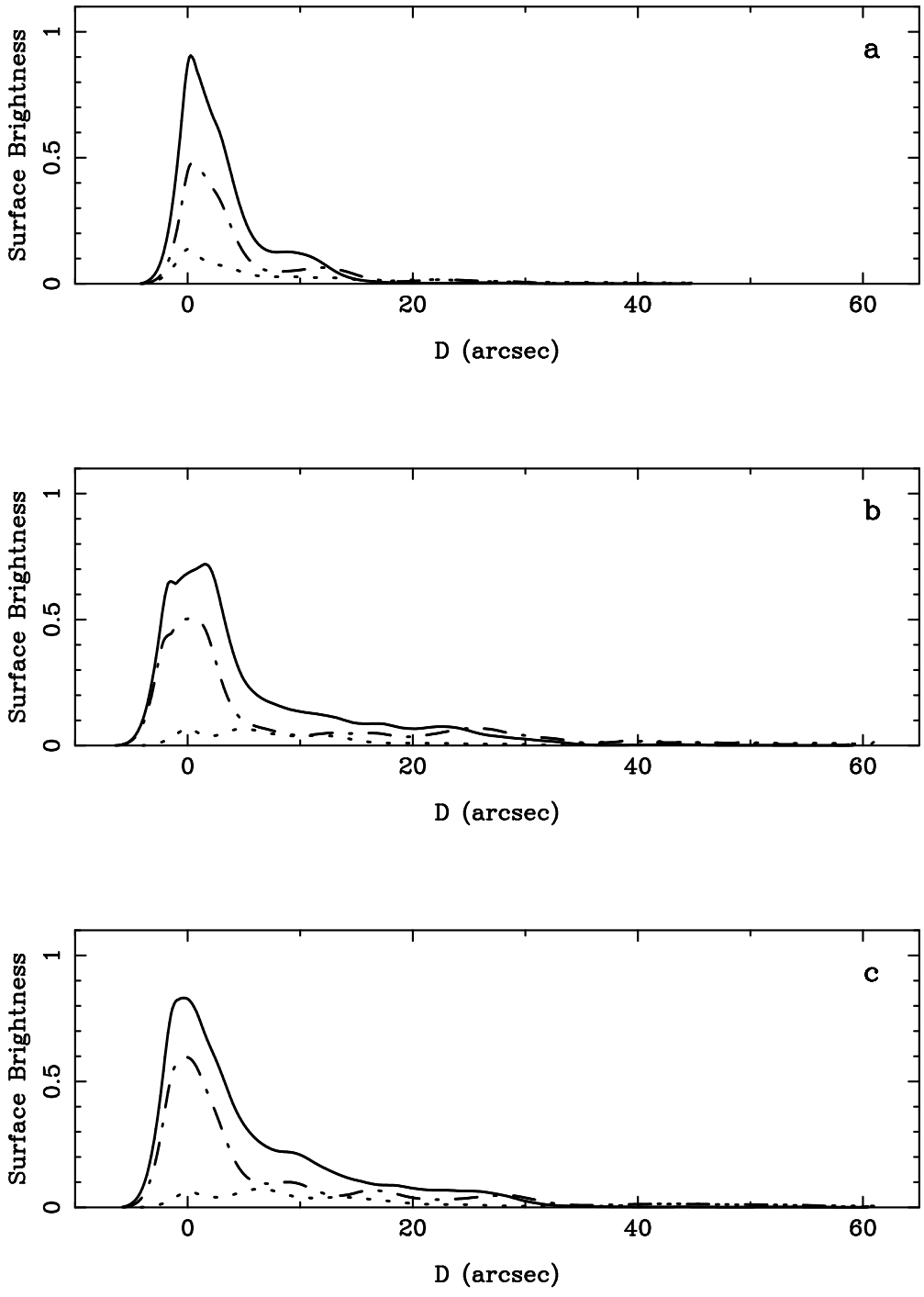


Fig. 24.— Average surface brightness at 151 MHz in a cross-sectional slice as a function of distance from the hot spot taking into account radiative losses. The radio emissivity is calculated supposing the relativistic electron density is proportional to the total pressure (full line), thermal pressure (dashed-dotted line) and the kinetic pressure (dotted line). Panels (a), (b) and (c) correspond to panels (c), (d) and (e) of Fig. 22, respectively.

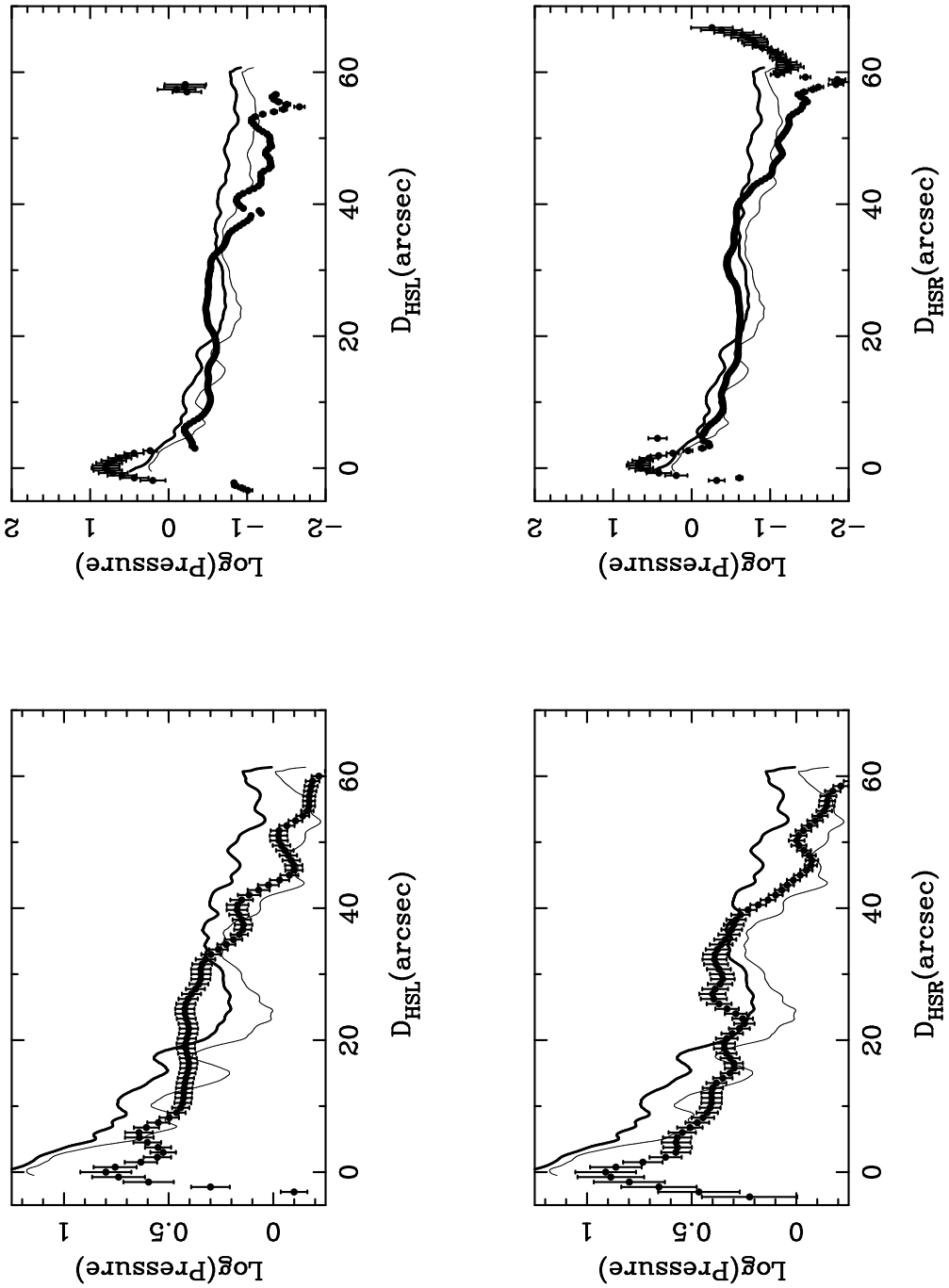


Fig. 25.— Comparison between the logarithm of the observed and calculated average total (thermal plus kinetic - thick line) and thermal (thin line) pressures as a function of distance from the hot spot for 151 MHz (left panels) and 1345 MHz (right panels). The Left side of the source is shown in the upper panels, and the Right side is shown in the lower panels. The calculated pressure is for an ambient density $n_a = 0.01$ cm^{-3}, and the units on the pressure are the same as in figure 12 for a value of the parameter b, defining the offset from minimum energy conditions, of 0.25. Thus, the unit on the 151 MHz pressure is 1.3×10^{-10} erg cm^{-3}, while that on the 1345 MHz pressure is 1.1×10^{-9} erg cm^{-3}.

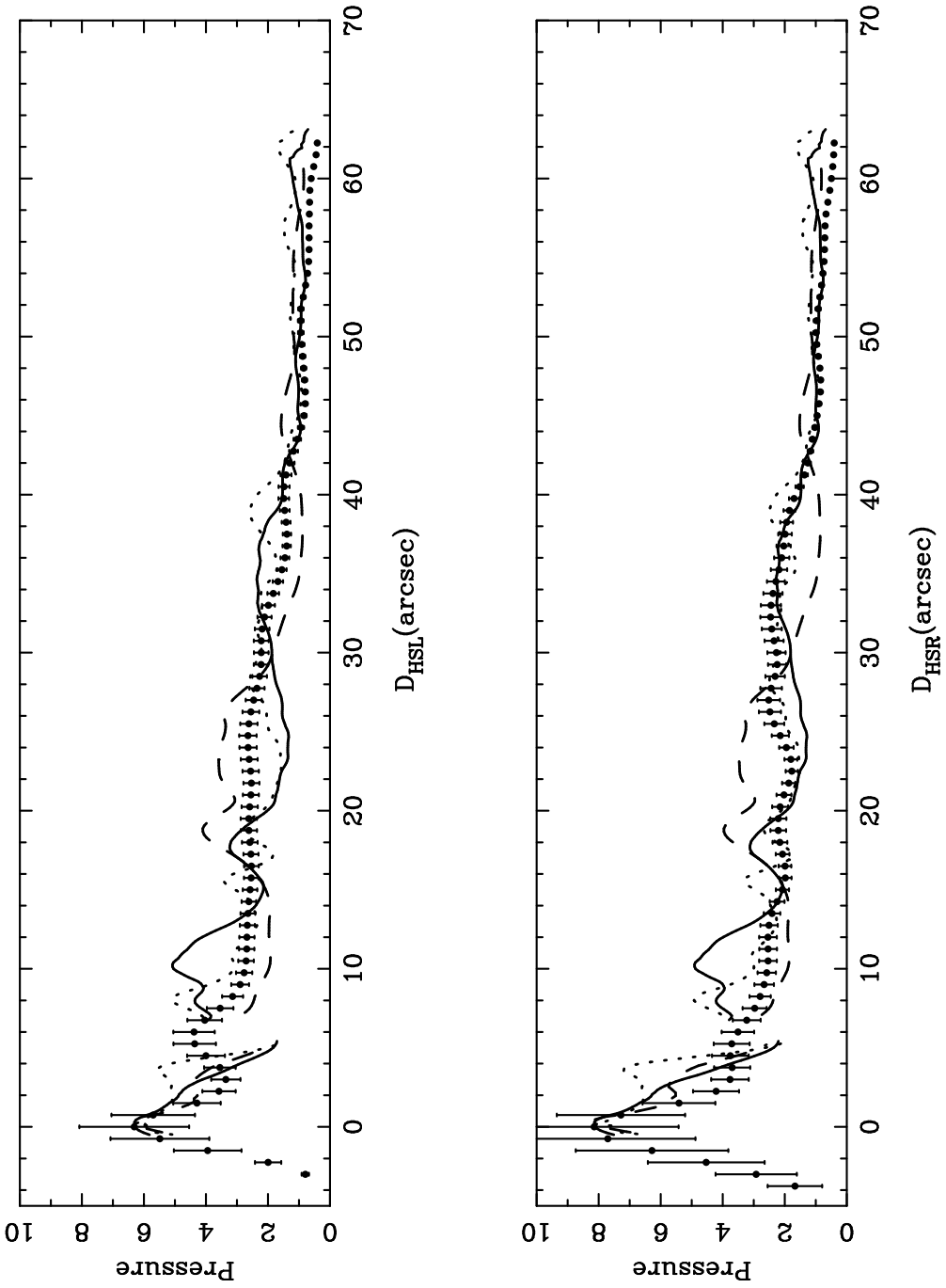


Fig. 26.— Comparison between observed and calculated average thermal pressure as a function of distance from the hot spot, with the numerical result scaled to match the empirical result at the hot spot peak. The Left side of the source is shown in the upper panel, and the Right side is shown in the lower panel. The dashed line, dotted line and full line correspond to panels (c), (d) and (e) of Fig. 22, respectively.

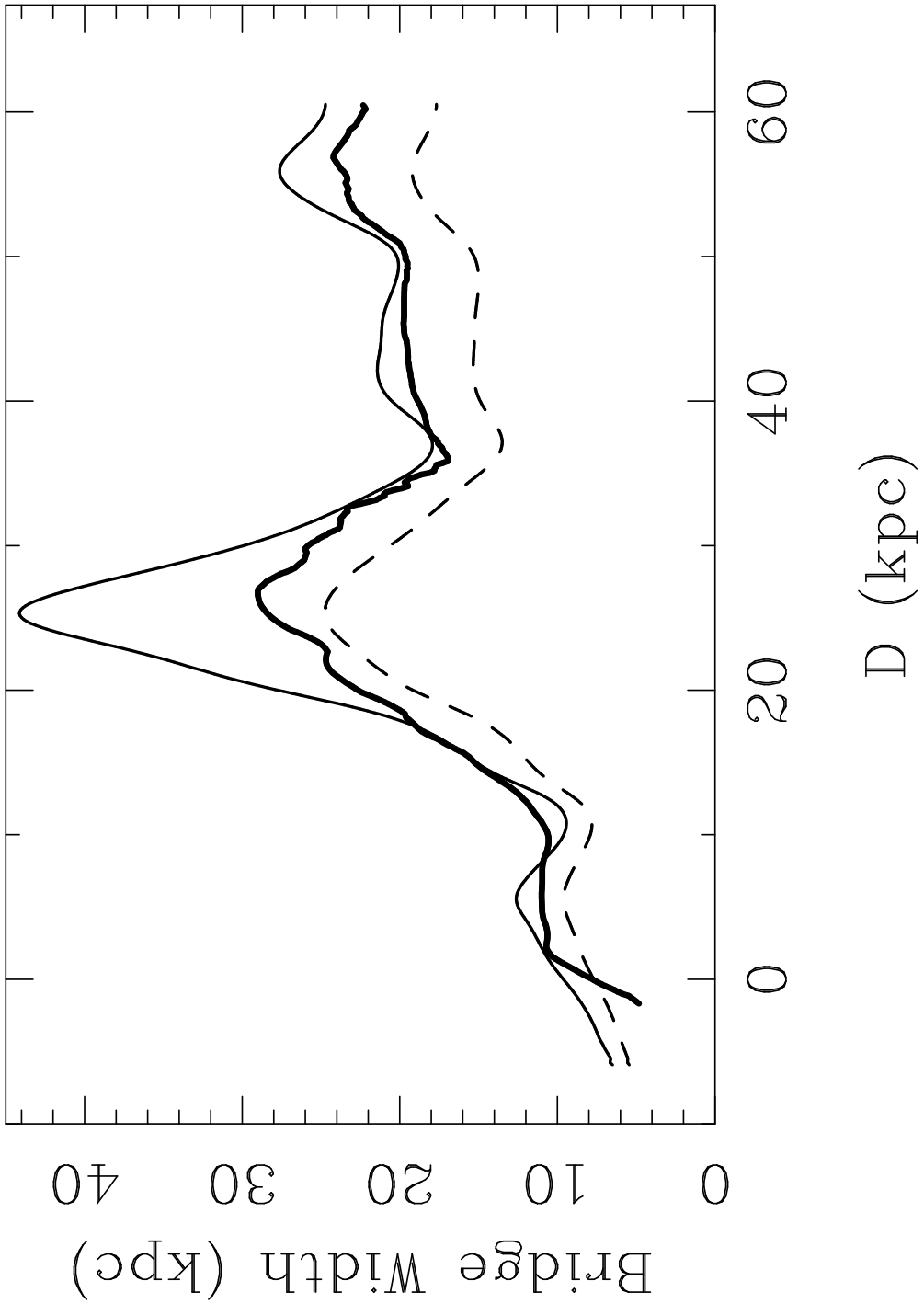


Fig. 27.— Bridge width calculated from the Gaussian fit (FWHM) and the second moment compared with the full width of the cocoon measured from the simulations as a function of distance from the hotspot. Thick line is cocoon (W), thin line is the Gaussian fit (W_G) and dashed line is the second moment (W_2).

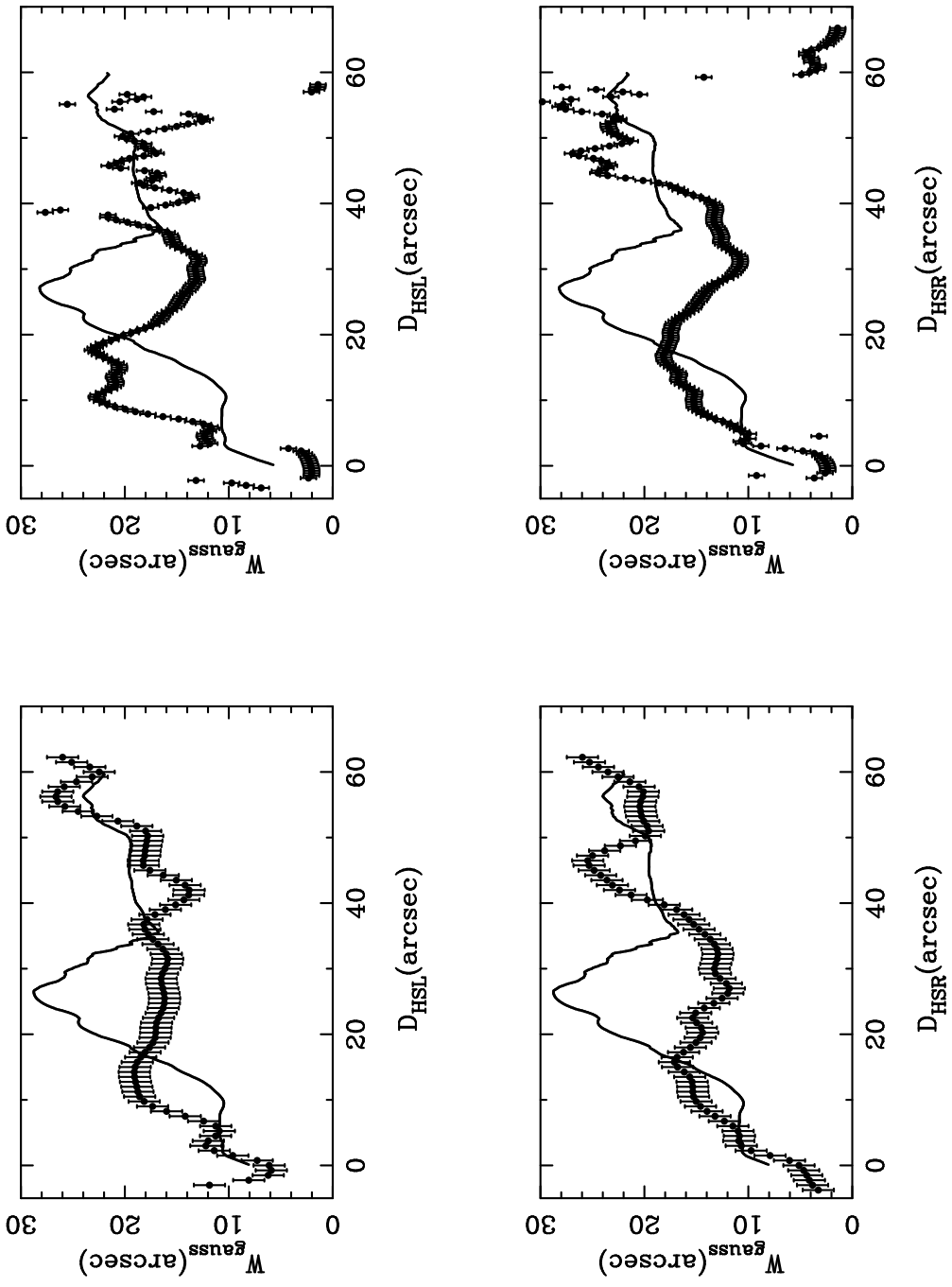


Fig. 28.— Comparison between the FWHM fit to the radio data with the "true" width of the simulated source as a function of distance from the hot spot for 151 MHz (left panels) and 1345 MHz (right panels). The Left side of the source is shown in the upper panels, and the Right side is shown in the lower panels.

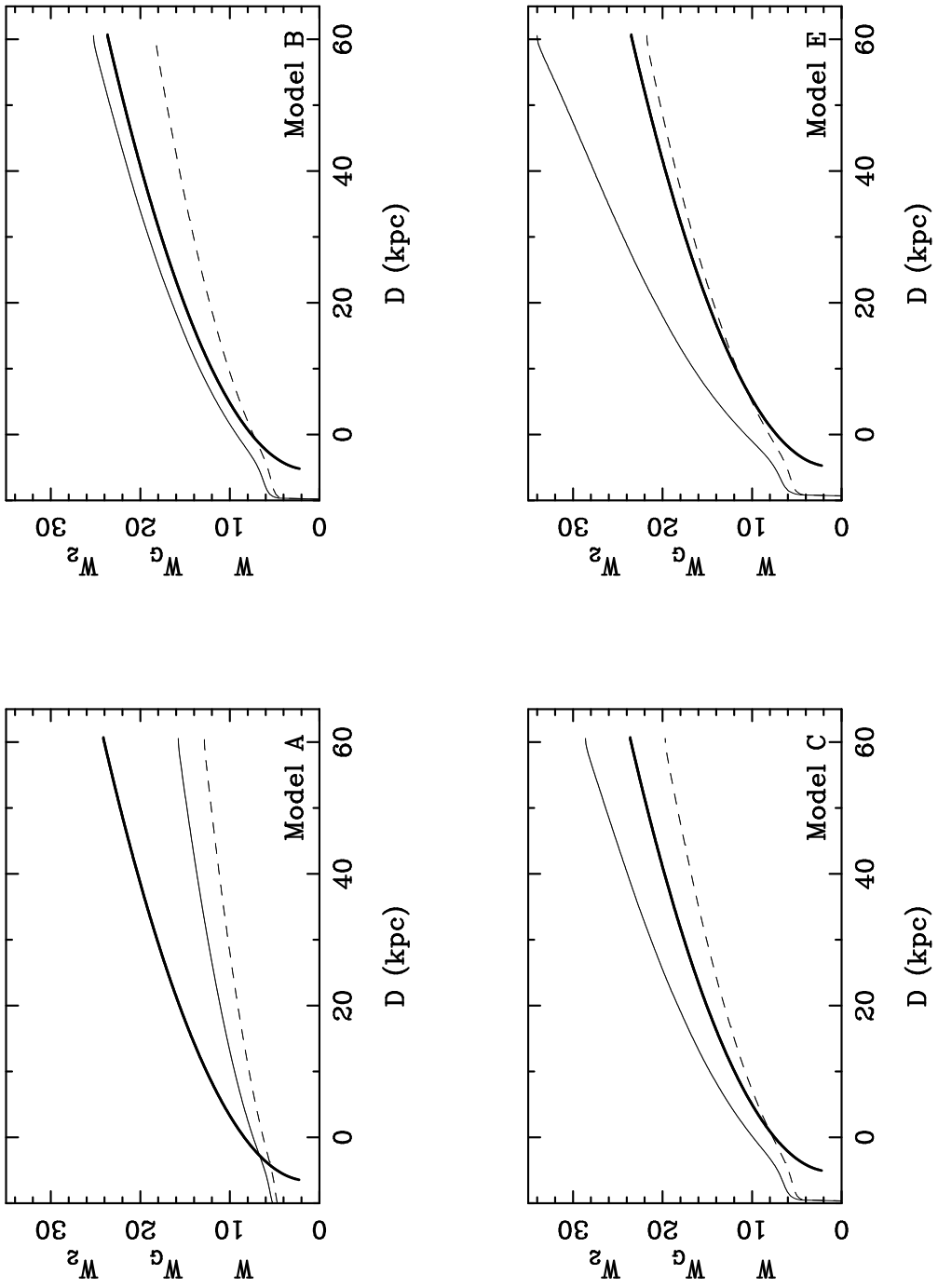


Fig. 29.— Bridge width calculated from the Gaussian fit (FWHM) and the second moment compared with the full width of the model cocoon as a function of distance from the hotspot. Thick line is cocoon (W), thin line is the Gaussian fit (W_G) and dashed line is the second moment (W_2). The four panels represents the models in Table 1.

This figure "f1.gif" is available in "gif" format from:

http://arxiv.org/ps/astro-ph/0406212v2

This figure "f2.gif" is available in "gif" format from:

http://arxiv.org/ps/astro-ph/0406212v2

This figure "f11.gif" is available in "gif" format from:

http://arxiv.org/ps/astro-ph/0406212v2

This figure "f12.gif" is available in "gif" format from:

http://arxiv.org/ps/astro-ph/0406212v2

This figure "f13.gif" is available in "gif" format from:

http://arxiv.org/ps/astro-ph/0406212v2

This figure "f14.gif" is available in "gif" format from:

http://arxiv.org/ps/astro-ph/0406212v2

This figure "f15.gif" is available in "gif" format from:

http://arxiv.org/ps/astro-ph/0406212v2

This figure "f16.gif" is available in "gif" format from:

http://arxiv.org/ps/astro-ph/0406212v2

This figure "f17.gif" is available in "gif" format from:

http://arxiv.org/ps/astro-ph/0406212v2

This figure "f18.gif" is available in "gif" format from:

http://arxiv.org/ps/astro-ph/0406212v2

This figure "f19.gif" is available in "gif" format from:

http://arxiv.org/ps/astro-ph/0406212v2

This figure "f20.gif" is available in "gif" format from:

http://arxiv.org/ps/astro-ph/0406212v2

This figure "f21.gif" is available in "gif" format from:

http://arxiv.org/ps/astro-ph/0406212v2

This figure "f22.gif" is available in "gif" format from:

http://arxiv.org/ps/astro-ph/0406212v2

This figure "f25.gif" is available in "gif" format from:

http://arxiv.org/ps/astro-ph/0406212v2

This figure "f26.gif" is available in "gif" format from:

http://arxiv.org/ps/astro-ph/0406212v2

This figure "f29.gif" is available in "gif" format from:

http://arxiv.org/ps/astro-ph/0406212v2

This figure "f30.gif" is available in "gif" format from:

http://arxiv.org/ps/astro-ph/0406212v2

This figure "f31.gif" is available in "gif" format from:

http://arxiv.org/ps/astro-ph/0406212v2

This figure "f32.gif" is available in "gif" format from:

http://arxiv.org/ps/astro-ph/0406212v2

This figure "f41.gif" is available in "gif" format from:

http://arxiv.org/ps/astro-ph/0406212v2

This figure "f44.gif" is available in "gif" format from:

http://arxiv.org/ps/astro-ph/0406212v2